


Article

# Surface-Bound and Volatile Mo Oxides Produced During Oxidation of Single MoS<sub>2</sub> Crystals in Air and High Relative Humidity

Robert Szoszkiewicz <sup>1,\*</sup> , Maciej Rogala <sup>2</sup> and Paweł Dąbrowski <sup>2</sup>

<sup>1</sup> Faculty of Chemistry, Biological and Chemical Research Centre, University of Warsaw, Żwirki i Wigury 101, 02-089 Warsaw, Poland

<sup>2</sup> Department of Solid State Physics, Faculty of Physics and Applied Informatics, University of Lodz, Pomorska 149/153, 90-236 Lodz, Poland

\* Correspondence: rszoszkiewicz@chem.uw.edu.pl

Received: 18 May 2020; Accepted: 6 July 2020; Published: 9 July 2020



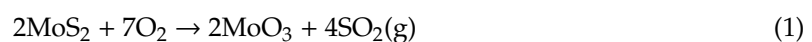
**Abstract:** We report on the MoO<sub>3</sub> oxides and their derivatives on microscopic 2H MoS<sub>2</sub> flakes oxidized in air and high relative humidity at a moderate temperature range below 410 °C. We combine XPS and AFM measurements such as topography, friction, creation of nanoscale ripples and scratches on the MoS<sub>2</sub> flakes deposited on Si substrates. We detect MoO<sub>3</sub> oxides mostly by measuring selected nanomechanical properties of the MoO<sub>3</sub> layer, such as its compressive mechanical stress at the plastic yield. We discuss basal surface coverage of the single MoS<sub>2</sub> flakes by the MoO<sub>3</sub> oxides. We discuss conditions for appearance of all possible MoO<sub>3</sub> oxide derivatives, such as molybdenum(VI) hydroxyoxides and MoO<sub>3</sub> hydrates. Our findings agree with an expected mechanistic switch in thermal oxidation in water vapors vs. air.

**Keywords:** MoS<sub>2</sub>; MoO<sub>3</sub>; surface science; nanoscale ripples; atomic force microscopy; XPS

## 1. Introduction

Naturally occurring MoS<sub>2</sub> crystals, molybdenites, have been widely used as solid lubricants [1]. The most common 2H molybdenite has three other polytypes: 3R, 1T and 1T', which differ in structure and electronic properties [2,3]. 2H and 3R molybdenites can be easily peeled off mechanically to yield atomically flat MoS<sub>2</sub> crystals with thickness down to one monolayer [2]. Easiness of mechanical exfoliation and semiconducting properties of 2H MoS<sub>2</sub> crystals have opened up a possibility to use them in a new generation of thin transistors [4]. Today, thin 2H MoS<sub>2</sub> crystals contribute tremendously to vigorous growth of flexible nanoelectronics, particularly in sensing, optoelectronics and energy harvesting [2,5–7]. In order to exploit all of these applications, the surface reactivity of single 2H MoS<sub>2</sub> microscopic flakes needs to be understood. The simplest and most widely applicable surface reactions pertain to their oxidation in ambient conditions and in the presence of water.

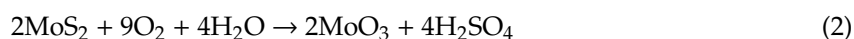
It has been confirmed both experimentally and theoretically that bulk MoS<sub>2</sub> oxidation is not readily observed at ambient conditions due to high energy barriers for such reactions [8–15]. Nevertheless, all kinds of thin and thick microscopic MoS<sub>2</sub> crystals are etched by oxygen within the time scales of minutes when heated to temperatures of at least 320 °C. Such etching progresses according to a following stoichiometry [8–12]:



Equation (1) states that out of all the possible Mo oxides, only the MoO<sub>3</sub> is produced. Exclusive presence of MoO<sub>3</sub> on the oxidized MoS<sub>2</sub> samples has been observed in many oxidative processes carried out in

oxygen or in air. Transparent MoO<sub>3</sub> crystals change into yellow and grayish-blue, only when oxygen defects yielding Mo<sup>5+</sup> and Mo<sup>4+</sup> species, respectively, are purposefully introduced, e.g., via hydrogen adsorption [16]. XPS and XRD experiments on thin Mo films have shown that all defective MoO<sub>3</sub> species with Mo<sup>4+</sup> and Mo<sup>5+</sup> became fully oxidized to MoO<sub>3</sub> already at more than 5% of oxygen in reactive gases [17]. The majority of the published studies, mostly using the XPS measurements, detect exclusively Mo<sup>6+</sup> oxides—i.e., MoO<sub>3</sub>, onto thermally oxidized MoS<sub>2</sub> samples [12,18,19]. Furthermore, by performing thermodynamic calculations and using enthalpies of bulk reactions, Walter et al. have calculated that for a closed system consisting of the MoS<sub>2</sub> crystals in air, Equation (1) is indeed an exclusive reaction pathway, but only till system temperature of 470 °C [12]. Above 470 °C, volatile (MoO<sub>3</sub>)<sub>3</sub> and (MoO<sub>3</sub>)<sub>4</sub> species started to appear in their simulations due to sublimation of the MoO<sub>3</sub>(s). At 525 °C none of the MoO<sub>3</sub> was predicted to stay on the oxidized MoS<sub>2</sub> samples.

Somewhat different MoS<sub>2</sub> oxidation outcomes, however, are expected in the presence of water or humid air. Ross and Sussman experimented with pulverized bulk MoS<sub>2</sub> crystals and showed that water vapors helped in producing substantially more MoO<sub>3</sub> than expected from Equation (1). They verified that an additional MoO<sub>3</sub> was produced in the course of a following reaction [20]:



Furthermore, volatile molybdenum(VI) hydroxyoxides, MoO<sub>2</sub>(OH)<sub>2</sub>(g), have been predicted to appear above 300 °C in the calculations of Walter et al. (There, partial pressure of water vapors was set to the saturated water vapor pressure at room temperature, or to 100% relative humidity at 25 °C (298K)) [12]. It is not clear whether MoO<sub>2</sub>(OH)<sub>2</sub> originated directly from water-mediated oxidation of the MoS<sub>2</sub> crystals or rather from water reacting with the MoO<sub>3</sub> adsorbed on the MoS<sub>2</sub> crystals, which seemed more likely. Noteworthy, bulk MoO<sub>3</sub> has been shown by inorganic chemistry books to dissolve slightly in water. Finally, yet other Mo species, the MoO<sub>3</sub> hydrates such as MoO<sub>3</sub>·H<sub>2</sub>O, have been recently suggested to appear on the MoS<sub>2</sub> crystals after their immersion in water for many hours [21].

Not only is the chemistry of the MoO<sub>3</sub> complicated, but its appearance and surface distribution on microscopic 2H MoS<sub>2</sub> crystals are elusive too. In the case of very thin MoS<sub>2</sub> flakes some loose islands of the MoO<sub>3</sub> oxides have been presumably observed directly in the AFM topographs overlaid with AFM-based magnetic force imaging [9]. Therein, MoO<sub>3</sub> was reported to be a non-magnetic material. In one of our earlier AFM and micro-Raman studies we pointed out that during initial 10–15 min of heating at temperatures ranging from 320 to 390 °C, in air, a predominantly observed outcome on thick microscopic MoS<sub>2</sub> flakes was triangular etch pits within the basal MoS<sub>2</sub> surface [11]. Similar triangular etch pits were observed several years earlier on very thin MoS<sub>2</sub> samples heated either in oxygen or in oxygen/argon flow or in air [8–10]. In all of those studies a typical depth of triangular etch pits was exactly one MoS<sub>2</sub> monolayer; i.e., 0.7 nm. Beyond triangular etch pits, very few morphological changes of the MoS<sub>2</sub> flakes have been noticed [11]. Since MoO<sub>3</sub> crystals are transparent, it is not clear whether MoO<sub>3</sub> stayed with those samples at all and/or covered the pits and a surrounding area uniformly. Particularly, almost the same thickness is expected for the MoO<sub>3</sub> and MoS<sub>2</sub> single layers [22–24].

It is not only difficult to detect MoO<sub>3</sub> via its physical properties, but according to our knowledge, none of the published results provided a direct chemical proof of the local MoO<sub>3</sub> existence on a single microscopic 2H MoS<sub>2</sub> flake. Typical XPS measurements are not so local and encompass at least several MoS<sub>2</sub> flakes. Raman measurements do not help either. The majority of the published Raman studies show either miniscule shifts of the Raman modes fingerprinting the MoS<sub>2</sub> crystals, i.e., the A<sub>1g</sub> and E<sub>12g</sub> modes [10,11], or an exclusive presence of the MoO<sub>3</sub> crystals on fully oxidized single 2H MoS<sub>2</sub> flakes [8]. This is likely due to a very small thickness of the oxide layer. Overall, the MoO<sub>3</sub> layers produced during gentle oxidation of single 2H MoS<sub>2</sub> crystals are transparent, thin and difficult to be differentiated both physically and chemically from an underlying MoS<sub>2</sub> substrate. In addition, such MoO<sub>3</sub> layers might contain MoO<sub>3</sub> derivatives, such as molybdenum(VI) hydroxyoxides and/or MoO<sub>3</sub> hydrates. Clearly, proper identification and surface distribution of the MoO<sub>3</sub> species and their derivatives on single 2H MoS<sub>2</sub> flakes deserve substantially more attention.

In this study we detected and differentiated the MoO<sub>3</sub> oxides and their derivatives from an underlying MoS<sub>2</sub> crystal on single and microscopic 2H MoS<sub>2</sub> flakes. We used a series of the MoS<sub>2</sub> samples, which were oxidized gently, each one at a different temperature between 205 to 410 °C, in dry or humid air. First, using XPS measurements we show how the content of the MoO<sub>3</sub> species on the MoS<sub>2</sub> samples changes with oxidization temperature. Next, by carefully manipulating AFM tips we created nanoscale ripples within the MoO<sub>3</sub> layer and scratched them out from single MoS<sub>2</sub> flakes. We related the thickness of the scratched out MoO<sub>3</sub> layer to its structure and used a model for formation of nanoscale ripples to obtain its compressive breaking strength. Next, we proved that oxidation on the edges of the MoS<sub>2</sub> crystals provides most of the needed MoO<sub>3</sub> to cover the MoS<sub>2</sub> flakes. Finally, we study sublimation of the MoO<sub>3</sub> oxide layer and its formation in high relative humidity conditions.

## 2. Materials and Methods

**Preparation of MoS<sub>2</sub> flakes:** Laboratory grade 2H molybdenite crystals were bought from SPI Supplies, West Chester, PA, USA, catalogue number #429MM-AB. The MoS<sub>2</sub> samples have been mechanically exfoliated using a standard double-sided scotch tape and transferred on fine polished and basically undoped <111> Si crystals with resistivity more than 10,000 Ω cm, bought from ITME, Warsaw, Poland. Prior to a sample transfer, the Si substrates were ultrasonically cleaned with acetone and isopropanol and dried with pure N<sub>2</sub>. Due to subsequent heating studies at temperatures of more than 300 °C, no annealing nor other cleaning methods have been used to remove any remaining traces of the scotch tape from the Si substrates. For sample heating in air we used a standard hot plate covered with a quartz Petri dish to insure a controlled atmosphere and proper distribution of temperatures within a heating zone. After calibrating the hotplate with a standard thermocouple and a Pt thermometer, we established a temperature error of ±2K on the sample surface. For experiments in high relative humidity we used a custom-built chemical reactor.

**X-ray photoelectron spectroscopy (XPS):** XPS was conducted in the multi chamber ultrahigh vacuum system (manufactured by Omicron Nanotechnology, Taunusstein, Germany) equipped with a hemispherical energy analyzer Phoibos 150 (manufactured by SPECS, Berlin, Germany) with a 2D-CCD detector. DAR 400 X-ray lamp with a non-monochromatic radiation of 1253.64 eV (Mg Kα) was used. The spectra for analysis of chemical shifts in Mo 3d core lines were collected with pass energy of 30 eV in “Fixed Analyzer Transmission” mode. For the peak fitting procedure, the CasaXPS (v.2.3, Casa Software Ltd., Teignmouth, UK) software was used. To ensure repeatability of the analysis of all samples, the same set of components with fixed energy separation was used for each of them. The binding energies of the measured spectra were calibrated to the C 1s core line position at 285 eV. For all of the investigated samples, an observed charging effect did not exceed 2 eV and no hardware charge compensation was needed.

**Atomic force microscopy (AFM):** Non-contact/tapping AFM imaging was conducted at amplitudes of several tens of nanometers with AC-160TSA-R3 cantilevers from Olympus, Tokyo, Japan using Cypher-S AFM manufactured by Asylum Research, Goleta, CA, USA. Contact mode AFM imaging was conducted with MLCT-E and/or MLCT-F cantilevers from Bruker, Santa Barbara, CA, USA and using Dimension Icon AFM manufactured by Bruker. We collected raw topography and lateral force microscopy (LFM) images of the investigated MoS<sub>2</sub> flakes. The images were collected with at least 256 points per line and treated with Gwyddion (v.2.51, Czech Metrology Institute, Brno, Czech Republic) software [25]. On topography images we removed glitches and used standard line-by-line first or second-order flattening and three-point plane levelling methods. No other image treatment and/or conditioning was performed.

Lateral spring constant calculations for AFM cantilevers used for measurements of the compressive breaking strength. The value of the lateral stiffness  $k_{lat}$  for a triangular MLCT-E cantilever used to indent and scratch the oxidized MoS<sub>2</sub> crystals was calculated using the Neumeister and Ducker model [26]. Unless otherwise measured from optical microscopy images, we used manufacturer’s specifications for all the relevant variables; i.e., SiN<sub>x</sub> Young modulus of 304 GPa, Poisson ratio of 0.24,

thickness of a cantilever of  $0.60 \pm 0.05 \mu\text{m}$ , triangle opening angle of  $28 \pm 2^\circ$  (measured), length of cantilever's arms from the base towards the point they meet of  $105 \pm 5 \mu\text{m}$  (measured), distance from the tip to the edge of a cantilever  $4 \pm 1 \mu\text{m}$ , width of cantilever arms of  $18 \pm 1 \mu\text{m}$  (measured) and tip's height of  $7 \pm 1 \mu\text{m}$ . Those values yielded  $k_{lat}$  of 54 N/m. Considering the errors of each parameters we obtained a minimum allowable  $k_{lat}$  of 25 N/m and a maximum of 116 N/m. These values of  $k_{lat}$  have been calculated using such a combination of parameters (with their errors) to obtain the lowest and the largest values of  $k_{lat}$ , respectively. Thus, we reported an average value within the errors; i.e.,  $k_{lat} = 71 \pm 45 \text{ N/m}$ . Using the Neumeister and Ducker approach, we also obtained a normal spring constant of 0.097 N/m, which is typical for the MLCT-E levers.

### 3. Results and Discussion

To investigate the presence of Mo oxides on the MoS<sub>2</sub> crystals, we prepared single 2H MoS<sub>2</sub> crystals on silicon/silica substrates, as explained in the Materials and Methods. We have studied flakes thicker than 10 nm, i.e., of more than 15 MoS<sub>2</sub> monolayers due to known dependencies of several physico-chemical properties of the MoS<sub>2</sub> flakes on their thickness, particularly for the flakes thinner than 10 monolayers [27]. First, the MoS<sub>2</sub> flakes were localized using light microscopy and AFM; see Figure 1. Next, we selected five samples with MoS<sub>2</sub> flakes for the XPS studies of their thermal oxidation. One of the samples served as our reference sample. Four other samples were separately heated on a hot plate for 10–15 min each: first at 320, second at 350, third at 370 and fourth at 410 °C.

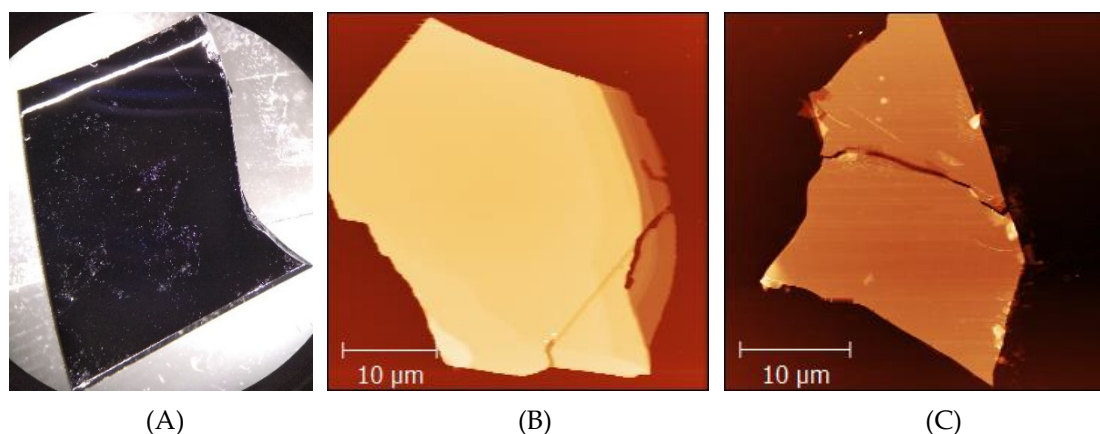


**Figure 1.** An exemplary sample containing agglomerates of mostly thick mechanically exfoliated 2H MoS<sub>2</sub> crystals on a silicon substrate. (A) An optical microscopy image of a typical sample being ca. 2 cm long and ca. 1.5 cm wide. Visible whitish spots are agglomerates of single MoS<sub>2</sub> flakes. Two of such single MoS<sub>2</sub> flakes are presented in (B,C). Image (B) is an AFM topograph of a flake with a mean height of a central zone (excluding several lone MoS<sub>2</sub> pieces) of ca. 65 nm and a Z-scale of the image of 130 nm. (C) An AFM topograph of another flake with a mean height of a central zone of ca. 25 nm and a Z-scale of the image of ca. 65 nm. For images (B,C) brighter colors represent portions of the image, which are higher (Z-scale).

Figure 2 shows the results of our XPS investigations on the samples prepared and oxidized in air. The Mo 3d core line XPS spectra were used in order to probe an oxidation process. Each such XPS spectrum contains four maxima, which have been related to the presence of two different oxidation states of the Mo ions. The applied peak fitting procedure yielded the binding energies of each maxima at 229.0 eV, 232.2 eV, 232.8 eV and 236.0 eV, respectively. The first two maxima were related to the spin-orbit doublet (Mo 3d 5/2 and 3/2) of the Mo<sup>4+</sup> oxidation state, which is characteristic for the MoS<sub>2</sub> sample. The second two maxima were related to the presence of the Mo<sup>6+</sup> oxidation state doublet, which within our reaction conditions has been predicted to be characteristic of the MoO<sub>3</sub>. During peak fitting procedures, the Gaussian–Lorentzian peak shapes were used and the relative peak areas were

fixed to a 2:3 ratios for each set of the respective 3/2 and 5/2 pairs. This procedure and the resulting binding energies are consistent with previous works [12,18,19].

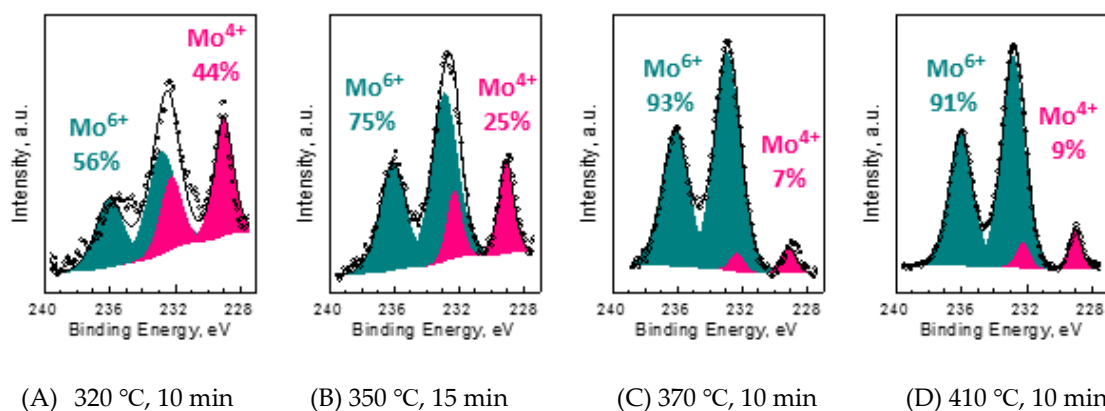


**Figure 2.** Our XPS results. (A–D) The XPS Mo 3d core line spectra of MoS<sub>2</sub> flakes heated in different temperatures presented together with the charts showing the concentrations of Mo<sup>4+</sup> and Mo<sup>6+</sup> ions within the surface layer of the flakes. The contributions coming from different oxidation states were fitted to the spectra and are presented in the charts below.

The oxidation of a single MoS<sub>2</sub> flake has been suggested to start already above 200 °C, as inferred from electronic density shifts within the MoS<sub>2</sub> monolayers via micro-Raman measurements [8]. However, earlier reports have shown through visualization of the obtained triangular etch pits that meaningful MoS<sub>2</sub> oxidation occurs in air only above 320 °C [8–11,28]. Such conclusions agree our XPS analysis in Figure 2. The presented results clearly show that during heating to a certain temperature the concentration of the Mo<sup>4+</sup> ions decrease, which is visible when comparing the spectra after heating at 320, 350 and 370 °C; see Figure 2A–C. However, somewhere above 370 °C this trend is stopped or even reversed, as is visible in the XPS spectra obtained after heating the sample in 410 °C; see Figure 2D. The XPS results, however, are averaged over an investigated area, which is typically between several tens to a hundred of μm<sup>2</sup>. Therefore, we decided to investigate the distribution of the Mo oxides on the surface of MoS<sub>2</sub> flakes using local AFM measurements.

After many trials and using high resolution, contact non-contact/tapping AFM imaging, we could not detect any obvious MoO<sub>3</sub> islands on and/or in the vicinity of the triangular etch pits on the XPS studied samples till heating them at 370 °C. We did not quit searching for the surface-bound MoO<sub>3</sub> layers on the prepared batch of samples; XPS results in Figure 2 clearly show the prevailing presence of oxides on the samples heated between 350 and 410 °C. Furthermore, the XPS results did not change upon sample annealing at 210 °C for 30 min, confirming that the Mo oxide stayed there even after annealing. This is why we decided to locally scratch several samples heated between 350 and 370 °C. Indeed, after several passages of a scanning AFM tip, we managed, at least in several cases, to break through a complete layer of the likely MoO<sub>3</sub> oxide after applying normal forces of up to several nN. While continuing the scratching process, we managed to remove any remaining pieces of the scratched layer and to expose a fresh basal plane of the Mo disulfide.

Figure 3 presents the results of removing a surface-bound MoO<sub>3</sub> oxide layer with help of an AFM tip. It shows the AFM recorded surface topography and corresponding lateral force microscopy (LFM) signals to visualize changes provoked on the sample during scratching. The investigated MoS<sub>2</sub> flake was ca. 30 nm thick. It was oxidized in five cycles of 10-minute heating at 350 °C and subsequent cooling to room temperature. The oxidized flake was continuously scratched in the zones denoted respectively by numbers “1”, “2”, “3” and “4” in Figure 3b. In the zone “1” the MoS<sub>2</sub> flake was rastered several times only, but it was enough to break continuity of the top oxide layer and produce lasting and visible indents in this layer. In the zones “2” and “3” the flake was scratched several more times than in “1,” so that visible surface ripples appeared within the oxidized MoS<sub>2</sub> surface. In the zone “4”

a portion of the MoS<sub>2</sub> flake was rescanned more than 10 times, resulting in a complete removal of an oxide layer.

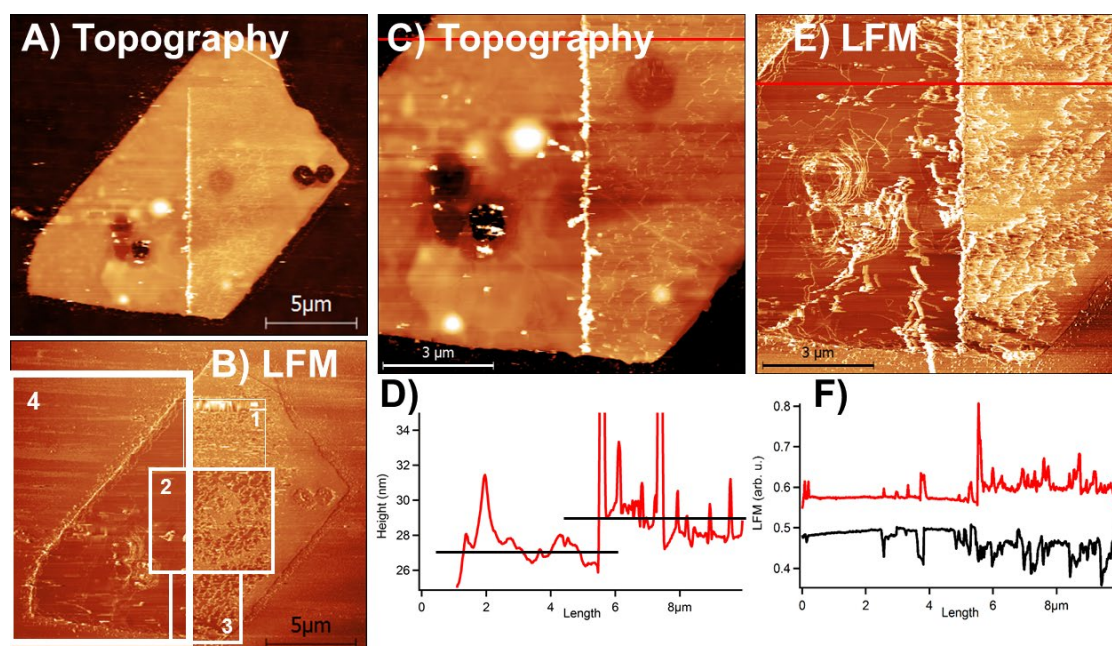


**Figure 3.** Removing the surface-bound MoO<sub>3</sub> oxide layer on a single MoS<sub>2</sub> flake with an AFM tip. The images show AFM recorded topography for (A,C) and uncalibrated friction (LFM signal) for (B,E). (B) shows that the flake was continuously scratched in zones 1, 2, 3 and 4 with a progressively increasing number of rescans between the zones. In the zone “4” the flake was rescanned more than 10 times, which produced complete removal of the oxide layer. (C) shows a close-up on the topography data from (A). (D) presents a topography cross-section line, marked in red in (C), to show that a removed oxide layer was  $2 \pm 1$  nm thick. (E) shows an LFM signal corresponding to (C). (F) shows a friction loop along a cross-sectional line presented in red in (E). A friction loop is an LFM signal recorded in trace (R → L) and retrace (L → R) scanning. It corresponds to twice of the uncalibrated friction. For (A,C) brighter colors represent higher portions of the image (Z-scale), while for (B,E) brighter colors represent higher values of the lateral force microscopy (LFM) signal. Z-scale in (A) was 60 nm or (C) 43 nm.

AFM topographs cannot provide direct information about the local chemistry of the investigated samples. Nevertheless, with their help we can discuss the thickness of the scratched out MoO<sub>3</sub> layer. To start with, after averaging several cross-sectional lines in local surface topography in Figure 3c, we obtained that a removed oxide layer was  $2 \pm 1$  nm in height; see Figure 3d.

Next, we explain how an obtained thickness of the oxide layer corresponds to its structure. The most thermodynamically stable MoO<sub>3</sub> polymorph existing in nature is the  $\alpha$ -MoO<sub>3</sub> called molybdite. Refined molybdite crystal structure shows a true layered arrangement of the MoO<sub>6</sub> octahedra with an orthorhombic unit cell belonging to a *Pbnm* space group [24]. Any given MoO<sub>3</sub> layer is a double layer composed of MoO<sub>6</sub> octahedra at two height levels. Within each level the MoO<sub>6</sub> octahedra are connected by shared lateral ends only. Connections between a ground level and an upper level are realized by sharing one edge between any two octahedra from ground and upper levels, respectively. Such an arrangement yields an overall height of a single  $\alpha$ -MoO<sub>3</sub> layer, *h*, it being 3/2 of the height of a single MoO<sub>6</sub> octahedron plus any necessary spacing between the layers. Consequently, we estimate *h* to be ca. 0.8 nm [24]. On the other hand, we can also estimate the value of *h* differently. To provide for dense spatial packing within the  $\alpha$ -MoO<sub>3</sub> structure, a second (upper)  $\alpha$ -MoO<sub>3</sub> layer is laterally shifted with respect to a first (lower) layer, but a third MoO<sub>3</sub> layer is positioned like a first layer. Such an arrangement yields the height of a respective  $\alpha$ -MoO<sub>3</sub> unit cell stretching from first to

third layer to be 1.4 nm. The thickness of an  $\alpha$ -MoO<sub>3</sub> monolayer atop another  $\alpha$ -MoO<sub>3</sub> monolayer is half of this value; i.e., 0.7 nm. Again, a slightly larger value is expected for the height of the  $\alpha$ -MoO<sub>3</sub> monolayer on the 2H MoS<sub>2</sub> crystal due to non-matching lateral dimensions between  $\alpha$ -MoO<sub>3</sub> and 2H MoS<sub>2</sub>. Thus, the expected thickness of a single MoO<sub>3</sub> layer atop the MoS<sub>2</sub> basal surface is between 0.7 and 0.8 nm, which makes it extremely close to the thickness of a single MoS<sub>2</sub> monolayer of ca. 0.7 nm. Consequently, the detected thickness of the MoO<sub>3</sub> layer corresponds to something between one to four MoO<sub>3</sub> monolayers.

Another important difference between MoS<sub>2</sub> crystals and detected MoO<sub>3</sub> oxide layers observed in Figure 3e,f is the substantially larger, ca. 1.5 times larger, friction on the surface containing rippled oxides comparing to a cleaned MoS<sub>2</sub> surface. A substantial friction increase was expected on the oxidized vs. pristine MoS<sub>2</sub> surface. MoS<sub>2</sub> surfaces are known for low friction and their moderately hydrophobic behavior acquired from the pristine MoS<sub>2</sub> surface after its quick passivation by hydrocarbons [29]. On the contrary, Mo oxides and their derivatives are strongly hydrophilic, which facilitates formation of water capillary bridges between these surfaces and a scanning AFM tip in ambient conditions. Such capillary bridges are known to account for substantial friction increase in air [30–32].

The results are presented in Figure 3, and more of such results together with accompanying high resolution XPS spectra, presented in the Supplementary Materials (Figures S1 and S2), confirm that the Mo oxide layer can be indented and scratched away from MoS<sub>2</sub> basal planes of single MoS<sub>2</sub> crystals. Let  $\sigma_{MoO_3}$  denote the compressive mechanical stress at the plastic yield of that layer. It is also referred to as the compressive breaking strength. The value of  $\sigma_{MoO_3}$  can be estimated from our experimental results presented in Figure 3b using the Dugdale model of pressure-induced formation of cracks in solid surfaces [33], which was adopted for conditions of indenting a material with a scanning AFM tip [34]. In brief, the model assumes that a scanning AFM tip performs a stick-and-slip motion between the cracks, which are generated just underneath the very surface of a material and become visible within the indents within the material created by an AFM tip. Any given indent grows when a tip of an AFM cantilever “sticks” to it by exerting a normal load. At the same time the tip shifts laterally in the process of surface scanning. Thus, the tip will “slip” by the lateral distance,  $\Delta$ , to a new indentation point once mechanical energy stored in the cantilever, due to its increasing lateral bending, exceeds the tip-material surface energy over the contact area. The value of  $\Delta$  is later measured as the distance between consecutive indents. The lateral length of a given indent within a material is denoted as  $\delta_t$ . The local breaking strength of a material,  $\sigma$ , is calculated from a following equation:

$$\sigma = (0.5 \cdot \Delta^2 \cdot k_{lat}) / (1.2 \cdot 2 \cdot \pi \cdot R \cdot (D + H) \cdot \delta_t) = 0.0663 \cdot \Delta^2 \cdot k_{lat} / (R \cdot (D + H) \cdot \delta_t) \quad (3)$$

In Equation (3),  $D$  is the depth of a crack;  $H$  is the height of a material pile removed during indentation within a crack;  $R$  is the tip curvature radius of an AFM cantilever and  $k_{lat}$  is its lateral (elastic) stiffness.

After careful examination of the zones “1” and “2” in Figure 3b we have observed that the values of  $\Delta$  and  $\delta_t$  are similar and typically equal several hundreds of nanometers. Following this observation we simplify Equation (3) to yield:  $\sigma_{MoO_3} = 0.0663(\Delta \cdot k_{lat}) / (R \cdot (D + H))$ . The values of  $(D + H)$  are limited in our case by a small thickness of an oxide layer. We have estimated  $(D + H) = 5 \pm 2$  nm; see Figure 3b. For the used here MLCT-E cantilever,  $R$  was estimated as  $50 \pm 10$  nm and  $k_{lat} = 71 \pm 45$  N/m was obtained, as explained in the Materials and Methods. Consequently, we obtained values of  $\sigma_{MoO_3}$  between 0.3 and 7.8 GPa. An upper limit of ca. 8 GPa is likely overestimated, since our values of  $(D + H)$  are smaller than in the case of a thick MoO<sub>3</sub> layer.

The value of  $\sigma_{MoO_3}$  can be explained quite well using some previously published data and our experimental details. We did not find the value of  $\sigma_{MoO_3}$  in the literature; however, the MoO<sub>6</sub> octahedra within each single MoO<sub>3</sub> layer are slightly deformable under pressure along one of the lateral directions [24]. On the contrary, the MoS<sub>2</sub> surface exhibits nice honeycomb lattices within each of the respective S and Mo-planes, which are not easy to break through [22,23]. Thus, one expects the value of  $\sigma_{MoO_3}$  to be much lower than a respective value of  $\sigma_{MoS_2}$ . In fact, within our experimental conditions, we did not observe any breaking through the underlying MoS<sub>2</sub> layer under the maximum

loading forces applied. Those forces were of up to four times of the loads applied to generate scratches presented in Figure 3. Therefore, up to several-times-lower values of  $\sigma_{\text{MoO}_3}$  than  $\sigma_{\text{MoS}_2}$  are expected. Several published experimental and theoretical studies reported the values of  $\sigma_{\text{MoS}_2}$  between 20 and 30 GPa [35,36]. Consequently, our values of  $\sigma_{\text{MoO}_3}$  might indeed relate to the presence of thin  $\alpha\text{-MoO}_3$  layers. In conclusion, despite not being easily noticeable, a thin  $\alpha\text{-MoO}_3$  layer can be differentiated via creating surface ripples and scratching out the oxide layer via repetitive scanning on the  $\text{MoS}_2$  samples with appropriate AFM cantilevers.

Next, we address the origins of the Mo oxide layer, which deposits on the  $\text{MoS}_2$  surfaces. Etched triangular pits would account for only a very small amount of the produced oxides and there must be other sources of it. In Figure 4 one can see an example of the  $\text{MoS}_2$  flake with  $\text{MoS}_2$  monolayers of thickness between 15 and 20 depending on a position along the flake. The flake was imaged at ambient conditions just after 12 min of its thermal oxidation at 390 °C in air. One can clearly notice triangular etch pits within the basal surface of the flake in Figure 4a, and a clean area surrounding the bottom of the flake in Figure 4b.

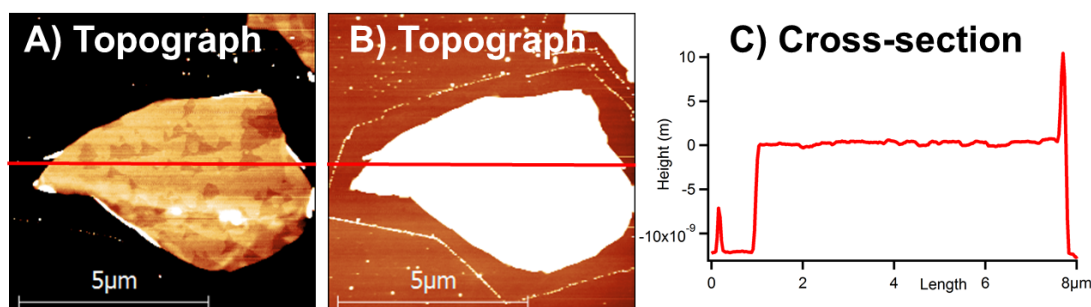


**Figure 4.** Etching and shrinking of a single  $\text{MoS}_2$  flake. (A,B) show topography images of the flake, with the Z-scale of several nanometers only in each. (A) is centered on a basal flake surface and (B) is centered on a surface of the silicon substrate. (C) presents a topographical cross-section taken laterally in a middle of the flake, as shown in A and B, in red. The flake is  $12 \pm 2$  nm thick.

The clean area around the  $\text{MoS}_2$  flake observed in Figure 4b has been freshly produced, since it contains no spots. This should be compared with many small spots visible on the Si substrate due to its prolonged handling in air. Thus, such a clean area must have originated from lateral shrinking of the flake during thermal oxidation. At the same time, not too many triangular etch pits were produced on this flake; see Figure 4a. Consequently, the amount of the Mo oxides produced by volumetric oxidation at edges of the flake must be substantially greater than the amount of oxides produced from its basal surface oxidation. Thus, oxidation on edges of the  $\text{MoS}_2$  flakes is a primary source of the  $\text{MoO}_3$ , particularly at heating temperatures of 350 °C and above. This result agrees with already published observations made by angle-resolved XPS, but on macroscopic  $\text{MoS}_2$  crystallites [37]. We have observed similar effects on many other  $\text{MoS}_2$  flakes, which were not too thick. On thick  $\text{MoS}_2$  flakes this effect is barely visible due to substantial volume of the  $\text{MoS}_2$  material enclosed within only slight shrinking of the lateral dimensions of such flakes due to heating.

Consequently, the only way to reconcile our data, i.e., volumetric oxidation, triangular surface etching and formation of an eventual thin Mo oxide layer, is to suggest that freshly-produced  $\text{MoO}_3$  must escape directly to the gas phase, but some portion of it can deposit back on the surface to form islands and even organized layers under appropriate conditions. In this sense, we have validated microscopically that the  $\text{MoO}_3$  produced through Equation (1) is initially in the gas form, at least within our experimental conditions.

Following the hypothesis that originally produced  $\text{MoO}_3$  goes to the gas phase first, we continued to notice that the amount of the  $\text{MoO}_3$  oxides, which are deposited back on the  $\text{MoS}_2$  surfaces, decreases as oxidation temperature rises above 370 °C; see Figure 3e. While more “energetic”—i.e., produced at higher temperatures— $\text{MoO}_3$  particles in the gas phase have less of a tendency for surface adsorption,



such results admit as well a possibility that the  $\text{MoO}_3$  particles, which have adsorbed on the surface, might quickly sublime at those conditions. Indeed, high quality  $\text{MoO}_3$  crystals grown on gold have been showed to sublime above  $400\text{ }^\circ\text{C}$  [38] and monolayers of amorphous  $\text{MoO}_3$  grown on  $\text{MoS}_2$  via  $\text{O}_2$  plasma exposure have sublimated completely at  $500\text{ }^\circ\text{C}$  [39]. Furthermore, thermodynamic calculations of Walter et al. [12] predicted  $\text{MoO}_3$  sublimation to start above  $470\text{ }^\circ\text{C}$ . Below, we provide an experimental proof for sublimation of the surface-bound  $\text{MoO}_3$  layers already at  $320\text{ }^\circ\text{C}$ .

Figure 5 presents an  $\text{MoS}_2$  flake heated for several minutes at  $370\text{ }^\circ\text{C}$  to promote oxidation and then left for about a month inside of a humid desiccator. In Figure 5a one can see an initial  $\text{MoS}_2$  flake. In Figure 5b one observes clearly some additional build-ups, likely  $\text{MoO}_3$  layers, which have deposited on various portions of the flake after its prolonged stay in desiccator. In Figure 5c one can notice that an entire oxide layer sublimated after the sample was heated at  $320\text{ }^\circ\text{C}$  for only four minutes. Such a low sublimation temperature does not compare even with lowest sublimation temperatures of  $400\text{ }^\circ\text{C}$  observed in the aforementioned studies [38]. However, one can quickly realize that the aforementioned  $\text{MoO}_3$  sublimation studies were conducted under vacuum and/or in highly controlled environments [38,39], whereas our results were obtained in far less clean conditions. In other words, surface adsorbed hydrocarbons and other surface contaminants on the pristine  $\text{MoS}_2$  surface might have prevented the formation of a well-organized and crystalline  $\text{MoO}_3$  layer. Alternatively, however, the slowly grown-up  $\text{MoO}_3$  layer might have contained some  $\text{MoO}_3$  derivatives, such as molybdenum(VI) hydroxyoxides and  $\text{MoO}_2(\text{OH})_2$ , which have been predicted to be formed, when water was present. If fact, the height of the formed  $\text{MoO}_3$  layer in Figure 5b is ca. 5 nm, which is much larger than thickness of the  $\text{MoO}_3$  layer obtained in air. This suggests slow formation of either an additional  $\text{MoO}_3$  in humid air due to Equation (2), or some additional  $\text{MoO}_2(\text{OH})_2$  species crystallizing on the sample. The  $\text{MoO}_2(\text{OH})_2$  species are far more volatile than a  $\text{MoO}_3$  layer [12] and sublime at lower temperature than  $\text{MoO}_3$ . We had no means to test for the presence of the hydroxyoxides on the  $\text{MoS}_2$  flake presented in Figure 5, but we decided to follow up on an unclear role of water in degradation and thermal oxidation of the  $\text{MoS}_2$  flakes.

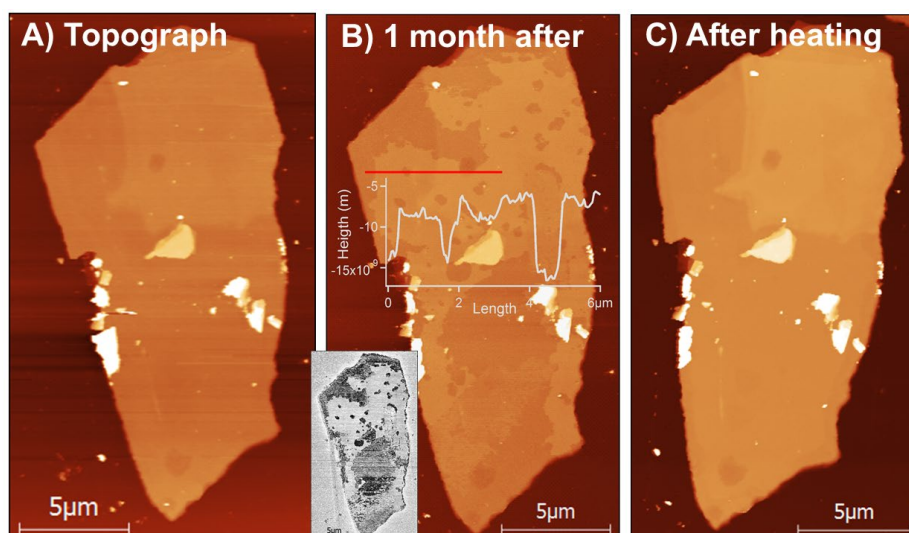


**Figure 5.** Sublimation of Mo oxide layers. (A) shows an initial  $\text{MoS}_2$  flake obtained by AFM imaging in non-contact mode. (B) presents additional build-ups, likely  $\text{MoO}_3$  layers, deposited on various portions of the flake after its short oxidation at  $370\text{ }^\circ\text{C}$  followed by one month stay in humid desiccator. A marked cross-sectional line (in red) shows that a typical thickness of an oxide layer is ca. 5 nm. Inset: corresponding AFM phase imaging, which seems to differentiate roughly oxidized (white) vs. non-oxidized (gray) portions of the flake, at least on a top part of the flake. (C) shows that the entire oxide layer sublimated after the sample was heated at  $320\text{ }^\circ\text{C}$  for only 4 minutes. Z-scale in (A) was 132 nm, in (B) 129 nm and in (C) 90 nm.

To start with, we investigated, again by AFM, the microscopic surface topography of several thermally oxidized MoS<sub>2</sub> samples after their submergence in water for the times ranging from a few minutes to several hours. We did not observe any topographical changes on those previously oxidized MoS<sub>2</sub> flakes. However, we could have incubated them in water for too little time in order to dissolve any MoO<sub>3</sub> oxide layers and/or create any etch pits in the MoS<sub>2</sub> [21]. Nevertheless, our results suggest that a thin layer of the MoO<sub>3</sub> species, which originated on surfaces of the oxidized MoS<sub>2</sub> flakes, prevented their further deterioration in water, at least within the time scale of several hours.

In order to start addressing the role of water during thermal oxidation of the single MoS<sub>2</sub> crystals from a different perspective, we decided to perform thermal oxidation at high relative humidity. One must acknowledge that our previous thermal oxidation studies above 300 °C, even in very humid air, occurred always at local relative humidity of being almost zero per cent. This is because the saturated water vapor pressure in vicinity of a hot surface,  $p_{sat}(T)$ , is a very strongly rising function of the temperature, so that any partial water pressure,  $p$ , in an open container in humid air produces a vanishingly small relative humidity,  $RH = p / p_{sat}(T)$ , above 200 °C. Thus, in order to study an effect of relative humidity in thermal oxidation of single MoS<sub>2</sub> flakes, one must utilize an enclosed chemical reactor, which assures the same pressure and relative humidity everywhere on the sample.

In Figure 6, we present the results of thermal oxidation of single MoS<sub>2</sub> crystals at  $RH = 80 \pm 7\%$ . The reaction was conducted within a custom-built chemical reactor. The sample was thermally oxidized for 5 min at mean pressure of 16 bar and mean temperature of 205 °C. It took 14 min to reach the reaction conditions and several more minutes to cool the reactor below 100 °C. A likely oxide layer was formed on the MoS<sub>2</sub> samples, because we were able to scratch this layer away (see Figure 6c) at similar forces as for the data presented in Figure 3. Furthermore, the measured thickness of the likely Mo oxide layer was  $2.2 \pm 0.2$  nm, which is also similar to the data presented in Figure 3.

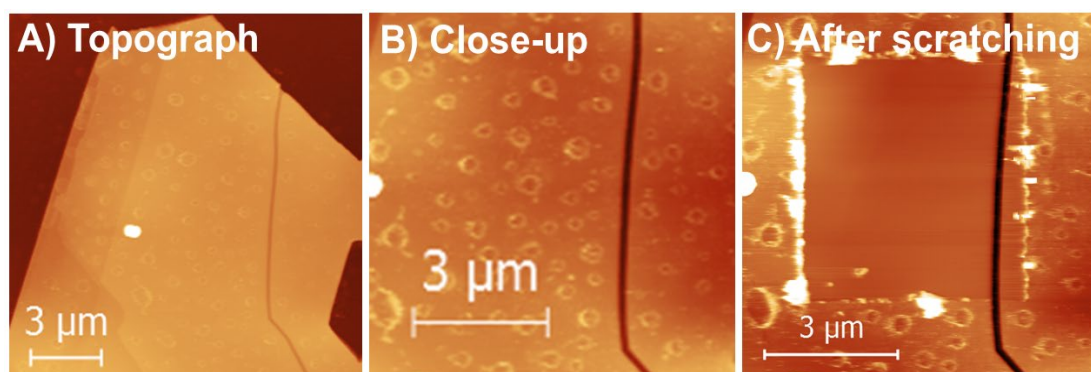


**Figure 6.** Thermal oxidation of a single MoS<sub>2</sub> flake at high relative humidity. (A,B) show AFM contact mode topography of an oxidized flake and a close-up on a particular spot, which was scratched out later, in (C). Flake thickness depending on a spot was between 90 to 100 nm. The flake was thermally oxidized for 5 min at  $RH = 80 \pm 7\%$  and at a mean temperature of 205 °C. An average thickness of the scratched out layer in (C) was  $2.2 \pm 0.2$  nm. Z-scales: (A) 274 nm; (B) 64 nm; (C) 42 nm.

One can notice that for thermal oxidation in air, when  $RH$  was almost zero, the MoO<sub>3</sub> oxides were not detected below 320 °C; see Figure 2. Thus, water must substantially accelerate oxidation at high relative humidity, as predicted by Equation (2). If water was acting only like a catalyst in Equation (1), then one would expect some associated triangular etch pits on the oxidized MoS<sub>2</sub> surface. However, for several samples and several scratches investigated within this study we observed no triangular etch pits within the oxidized MoS<sub>2</sub> layers and the underlying MoS<sub>2</sub> surface, i.e., within the scratch. Thus, water does indeed induce an additional oxidation pathway, as in Equation (2). In such a case, however, a thick MoO<sub>3</sub> layer would have been observed in Figure 6, which was not the case. Thus, the situation is likely more complicated.

One of the recently published studies suggested that water degrades MoS<sub>2</sub> crystals by partially dissolving them to yield pits and to produce non-transparent grains of insoluble crystals of the MoO<sub>3</sub> monohydrate, MoO<sub>3</sub>·H<sub>2</sub>O [21]. We have indeed observed some discoloration on the oxidized samples. Several MoO<sub>3</sub> hydrates have been characterized till now [40–42]; in particular, MoO<sub>3</sub>·*n*H<sub>2</sub>O with *n* = 2, 1, 1/2 and 1/3. Mono and di-hydrates have been found to be most stable structurally [40,41]. The MoO<sub>3</sub>·2H<sub>2</sub>O is most stable at room temperature and MoO<sub>3</sub>·H<sub>2</sub>O was found to exist between 60 to 140 °C. Above 140 °C the MoO<sub>3</sub> hydrates convert to α-MoO<sub>3</sub> [41]. We have conducted our experiments above 200 °C, i.e., where any hydrates shall already convert to oxides. The only way for them to appear in our experiments would be to form exclusively at room temperature or during reactor cooling. The MoO<sub>3</sub> hydrates, however, are typically produced via crystallization from slowly acidified solutions of molybdate ions [40–42]. Thus, in order for the MoO<sub>3</sub> hydrates to appear, the molybdate ions, such as MoO<sub>4</sub><sup>2-</sup>, need to be produced first. These anions are typically produced from reactions with MoO<sub>3</sub> in alkali solutions, which is not the case in our oxidation conditions. Consequently, we are of the opinion that no MoO<sub>3</sub> hydrates have been produced on MoS<sub>2</sub> in humid air.

Despite a predicted lack of the MoO<sub>3</sub> hydrates, we suggest that what it takes place in high relative humidity conditions is an accelerated production of the MoO<sub>3</sub> via Equation (2), as in bulk, but together with substantial conversion of the MoO<sub>3</sub> layer to volatile MoO<sub>2</sub>(OH)<sub>2</sub> species. Said hypothesis agrees with the following observations. Smolik et al. reported experimental data and thermodynamical calculations on oxidation, volatilization and re-deposition of molybdenum oxide species formed from a certain molybdenum alloy between 400 and 800 °C in flowing air [43]. The Mo oxide species on their Mo alloy underwent volatilization, which was dominated by the appearance of the MoO<sub>3</sub> above 550 °C and by the appearance of the MoO<sub>2</sub>(OH)<sub>2</sub>, formed from the small ingress of water vapor, at temperatures below 550 °C. Furthermore, within conditions closer to our experimental conditions Walter et al. [12] calculated that MoO<sub>2</sub>(OH)<sub>2</sub> is produced in thermal oxidation of the bulk MoS<sub>2</sub> crystals already at 300 °C. This is much earlier than in results of Smolik et al., but similarly to Smolik et al., also for a small ingress of water vapor. Thus, it is expected that at high relative humidity appearance, and fast volatilization of the MoO<sub>2</sub>(OH)<sub>2</sub> species occurs already at much lower temperatures than 300 °C. Consequently, at high relative humidity a crossover is expected from the MoS<sub>2</sub> oxidation governed by Equation (1) to oxidation governed by Equation (2), but together with formation and sublimation of the MoO<sub>3</sub> hydroxyoxides. In this way, large amounts of MoO<sub>3</sub> are produced quickly and a complete basal MoS<sub>2</sub> surface is transformed in Mo oxide species very fast, so that no triangular etch pits are observed. At the same time a large portion of the newly produced MoO<sub>3</sub> is converted into volatile MoO<sub>2</sub>(OH)<sub>2</sub> species, which leave the reaction environment. Overall, not much of the produced MoO<sub>3</sub> stays on the MoS<sub>2</sub> surface. However, systematic studies of thermal oxidation as a function of relative humidity and oxidation temperature are needed to address this hypothesis in detail.

Finally, we compare our results with laser-induced oxidation and thinning of MoS<sub>2</sub> crystals. To do so, we chose two seminal studies [44,45]. The first study discussed laser induced thinning and oxidation in air [44]. The other study was focused on laser-induced electrochemical thinning of the MoS<sub>2</sub> in electrochemical, although aqueous, solutions [45]. In none of these studies, however, have Mo oxides been detected. In [44] the Authors went to great lengths to exclude any MoO<sub>3</sub> presence via Raman, photoluminescence and electronic transport studies. Nevertheless, thin MoO<sub>3</sub> layers are not necessarily insulating [46] and micro-Raman studies have been notorious for not showing the local presence of MoO<sub>3</sub> layers [10,11]. A major reason for difficulty when trying to see any MoO<sub>3</sub> on the laser-oxidized MoS<sub>2</sub> flakes is certainly that laser-thinning studies are quite local. This means that only a tiny portion of each single MoS<sub>2</sub> flake is heated each time and extremely small amounts of the MoO<sub>3</sub> are produced. Furthermore, locally obtained temperatures achieved by laser heating of the MoS<sub>2</sub> surface are likely much above sublimation temperatures of the MoO<sub>3</sub> oxides. This is facilitated by poor (normal) thermal conductivity between subsequently stacked MoS<sub>2</sub> layers within a crystal. This effect, however, does not play a major role for globally heated MoS<sub>2</sub> samples, as in our case here. Thus, we expect different outcomes between laser-induced heating and thermally induced oxidation, and in

particular more of the MoO<sub>3</sub> staying on the samples oxidized thermally than in the laser-induced studies. Nevertheless, that all depends on particular experimental conditions. Consequently, it would be extremely interesting to extend the nanomechanical testing for the local presence of the MoO<sub>3</sub>, such as presented within our paper, to the laser-thinned MoS<sub>2</sub> samples.

#### 4. Conclusions

With help of XPS and AFM measurements we reported on microscopic details associated with the oxidation of thick MoS<sub>2</sub> flakes deposited on silicon at temperatures between 205 and 410 °C in dry and humid air. We observed for samples oxidized at 350 °C that triangular etch pits started to coexist with MoO<sub>3</sub> islands and layers. Above 370 °C the amount of MoO<sub>3</sub> detected on the MoS<sub>2</sub> surface started to decrease, most likely due to sublimation of the MoO<sub>3</sub> layers. The MoO<sub>3</sub> layers produced on the MoS<sub>2</sub> samples were usually not distinguishable morphologically from an underlying MoS<sub>2</sub> surface. However, the MoO<sub>3</sub> layers could be scratched away from an underlying MoS<sub>2</sub> surface with appropriate AFM cantilevers. We estimated breaking compressive strengths of the MoO<sub>3</sub> layer to be between 0.3 and 7.8 GPa. Our results agreed with two important aspects for thermal oxidation of the MoS<sub>2</sub> flakes. First, out of the several possible Mo oxides, we detected only the MoO<sub>3</sub> species. Second, we suggested that MoO<sub>3</sub> species had to be originally produced in the gas phase, and then only some of them adsorbed on the MoS<sub>2</sub> surface. MoO<sub>3</sub> adsorption has been most effective between 350 and 410 °C.

We also began to address the role of relative humidity in oxidation of the MoS<sub>2</sub> crystals. We showed that sublimation of the MoO<sub>3</sub> layers occurred already at 320 °C for the MoS<sub>2</sub> samples oxidized previously at 370 °C and then left alone to slowly anneal at humid ambient conditions. We suggested that this result could be due to the presence of the MoO<sub>3</sub> hydroxyoxides within thick MoO<sub>3</sub> layers. Next, we showed the results of thermal oxidization of the MoS<sub>2</sub> samples at high relative humidity of 80 ± 7% and mean temperature of only 205 °C. We observed quite dense layers of the likely Mo oxides, similarly to oxidation in air, but with no triangular etch pits within those layers and within an underlying MoS<sub>2</sub> surface. We explained such results by substantially faster MoS<sub>2</sub> oxidation in the presence of high relative humidity than in air and additional removal of the produced MoO<sub>3</sub> oxide due to their conversion into volatile molybdenum(VI) hydroxyoxide species.

**Supplementary Materials:** The following are available online at <http://www.mdpi.com/1996-1944/13/14/3067/s1>, Figure S1: An example of creating ripples and scratching out an already fragmented oxide layer (due to extensive heating). Left: topography; Right: twice the uncalibrated friction, Figure S2: Progression of the process of removing already loosely bound oxides from the flake in Figure S1. Presented are 6.6 µm by 6.6 µm AFM contact mode topography images.

**Author Contributions:** Conceptualization, R.S.; methodology, R.S.; validation, R.S., M.R., P.D.; formal analysis, R.S., M.R., P.D.; investigation, R.S., M.R., P.D.; resources, R.S., M.R., P.D.; data curation, R.S., M.R., P.D.; writing—original draft preparation, R.S., M.R., P.D.; writing—review and editing, R.S., M.R., P.D.; supervision, R.S.; project administration, R.S.; funding acquisition, R.S. All authors have read and agreed to the published version of the manuscript.

**Funding:** This research was funded by the National Science Center, Poland, grant number 2017/27/B/ST4/00697 (RSz) and grant number 2016/21/B/ST5/00984 (MR, PD), and by the UW Statuary Funds.

**Acknowledgments:** We are grateful to Wojciech L. Spychalski from Warsaw University of Technology for preparation of technical drawings for a chemical reactor used in high humidity studies and for his invaluable help in construction and testing of this reactor. We thank Krystian Lewkowicz for oxidizing the MoS<sub>2</sub> samples at high relative humidity within our chemical reactor and for collecting some AFM data on these samples. We acknowledge Kamil Węgrzyn for assisting in the AFM measurements presented in Figure 4.

**Conflicts of Interest:** The authors declare no conflict of interest.

#### References

1. Lince, J.R.; Fleischauer, P.D. Ch.7. In *Space Vehicle Mechanisms: Elements of Successful Design*; Conley, P., Ed.; Wiley-Interscience: New York, NY, USA, 1998.
2. Wang, Q.H.; Kalantar-Zadeh, K.; Kis, A.; Coleman, J.N.; Strano, M.S. Electronics and optoelectronics of two-dimensional transition metal dichalcogenides. *Nat. Nanotechnol.* **2012**, *7*, 699–712. [[CrossRef](#)] [[PubMed](#)]

3. Liu, L.; Wu, J.; Wu, L.; Ye, M.; Liu, X.; Wang, Q.; Hou, S.; Lu, P.; Sun, L.; Zheng, J.; et al. Phase-selective synthesis of 1T' MoS<sub>2</sub> monolayers and heterophase bilayers. *Nat. Mater.* **2018**, *17*, 1108–1114. [[CrossRef](#)] [[PubMed](#)]
4. Radisavljevic, B.; Radenovic, A.; Brivio, J.; Giacometti, V.; Kis, A. Single-layer MoS<sub>2</sub> transistor. *Nat. Nanotechnol.* **2011**, *6*, 147–150. [[CrossRef](#)]
5. Li, X.; Zhu, H. Two-dimensional MoS<sub>2</sub>: Properties, preparation, and applications. *J. Materiomics* **2015**, *1*, 33–44. [[CrossRef](#)]
6. Gong, C.; Zhang, Y.; Chen, W.; Chu, J.; Lei, T.; Pu, J.; Dai, L.; Wu, C.; Cheng, Y.; Zhai, T.; et al. Electronic and Optoelectronic Applications Based on 2D Novel Anisotropic Transition Metal Dichalcogenides. *Adv. Sci.* **2017**, *4*, 1700231. [[CrossRef](#)]
7. Gonzalez-Marin, J.F.; Unuchek, D.; Watanabe, K.; Taniguchi, T.; Kis, A. MoS<sub>2</sub> photodetectors integrated with photonic circuits. *2D Mat. Appl.* **2019**, *14*, 1–7. [[CrossRef](#)]
8. Yamamoto, M.; Einstein, T.L.; Fuhrer, M.S.; Cullen, W.G. Anisotropic Etching of Atomically Thin MoS<sub>2</sub>. *J. Phys. Chem. C* **2013**, *117*, 25643–25649. [[CrossRef](#)]
9. Wu, J.; Li, H.; Yin, Z.; Li, H.; Liu, J.; Cao, X.; Zhang, Q.; Zhang, H. Layer thinning and etching of mechanically exfoliated MoS<sub>2</sub> nanosheets by thermal annealing in air. *Small* **2013**, *9*, 3314–3319.
10. Zhou, H.; Yu, F.; Liu, Y.; Zou, X.; Cong, C.; Qiu, C.; Yu, T.; Yan, Z.; Shen, X.; Sun, L.; et al. Thickness-dependent patterning of MoS<sub>2</sub> sheets with well-oriented triangular pits by heating in air. *Nano Res.* **2013**, *6*, 703–711. [[CrossRef](#)]
11. Ukegbu, U.; Szoszkiewicz, R. Microscopic Kinetics of Heat-Induced Oxidative Etching of Thick MoS<sub>2</sub> Crystals. *J. Phys. Chem. C* **2019**, *123*, 22123–22129. [[CrossRef](#)]
12. Walter, T.N.; Kwok, F.; Simchi, H.; Aldosari, H.M.; Mohny, S.E. Oxidation and oxidative vapor-phase etching of few-layer MoS<sub>2</sub>. *J. Vac. Sci. Technol. B* **2017**, *35*, 021203. [[CrossRef](#)]
13. Rao, R.; Islam, A.E.; Campbell, P.M.; Vogel, E.M.; Maruyama, B. In situ thermal oxidation kinetics in few layer MoS<sub>2</sub>. *2D Mater.* **2017**, *4*, 025058. [[CrossRef](#)]
14. Wang, G.; Pandey, R.; Karna, S.P. Physics and chemistry of oxidation of two-dimensional nanomaterials by molecular oxygen. *WIREs Comput. Mol. Sci.* **2017**, *7*, 1–16. [[CrossRef](#)]
15. Santosh, K.; Longo, R.; Wallace, R.; Cho, K. Surface oxidation energetics and kinetics on MoS<sub>2</sub> monolayer. *J. Appl. Phys.* **2015**, *117*, 135301.
16. Alves de Castro, I.; Datta, R.S.; Ou, J.Z.; Castellanos-Gomez, A.; Sriram, S.; Daeneke, T.; Kalantar-zadeh, K. Molybdenum Oxides – From Fundamentals to Functionality. *Adv. Mater.* **2017**, *29*, 1701619. [[CrossRef](#)]
17. Bihn, J.-H.; Park, J.; Kang, Y.-C. Synthesis and Characterization of Mo Films Deposited by RF Sputtering at Various Oxygen Ratios. *J. Korean Phys. Soc.* **2011**, *58*, 509–514. [[CrossRef](#)]
18. Ko, T.Y.; Jeong, A.; Kim, W.; Lee, J.; Kim, Y.; Lee, Y.E.; Ryu, G.H.; Park, K.; Kim, D.; Lee, Z.; et al. On-stack two-dimensional conversion of MoS<sub>2</sub> into MoO<sub>3</sub>. *2D Mater.* **2017**, *4*, 014003. [[CrossRef](#)]
19. Hussain, S.; Singh, J.; Vikraman, D.; Singh, A.K.; Iqbal, M.Z.; Khan, M.F.; Kumar, P.; Choi, D.-C.; Song, W.; An, K.-S.; et al. Large-area, continuous and high electrical performances of bilayer to few layers MoS<sub>2</sub> fabricated by RF sputtering via post-deposition annealing method. *Sci. Rep.* **2016**, *6*, 30791. [[CrossRef](#)]
20. Ross, S.; Sussman, A. Surface Oxidation of Molybdenum Disulfide. *J. Phys. Chem.* **1955**, *59*, 889–892. [[CrossRef](#)]
21. Zhang, X.; Jia, F.; Yang, B.; Song, S. Oxidation of Molybdenum Disulfide Sheet in Water under in Situ Atomic Force Microscopy Observation. *J. Phys. Chem. C* **2017**, *121*, 9938–9943. [[CrossRef](#)]
22. Dai, Z.; Jin, W.; Grady, M.; Sadowski, J.T.; Dadap, J.I.; Osgood, R.M., Jr.; Pohl, K. Surface structure of bulk 2H-MoS<sub>2</sub>(0001) and exfoliated suspended monolayer MoS<sub>2</sub>: A selected area low energy electron diffraction study. *Surf. Sci.* **2017**, *660*, 16–21. [[CrossRef](#)]
23. Kadantsev, E.S.; Hawrylak, P. Electronic structure of a single MoS<sub>2</sub> monolayer. *Solid State Comm.* **2012**, *152*, 909–913. [[CrossRef](#)]
24. Asbrink, S.; Kihlberg, L.; Malinowski, M. High-Pressure Single-Crystal X-ray Diffraction Studies of MoO<sub>3</sub>. I. Lattice Parameters up to 7.4 GPa. *J. Appl. Crystallogr.* **1988**, *21*, 960–962. [[CrossRef](#)]
25. Nečas, D.; Klapetek, P. Gwyddion: An open-source software for SPM data analysis. *Cent. Eur. J. Phys.* **2012**, *10*, 181–188. [[CrossRef](#)]
26. Neumeister, J.M.; Ducker, W.A. Lateral, normal, and longitudinal spring constants of atomic-force microscopy cantilevers. *Rev. Sci. Instrum.* **1994**, *65*, 2527–2531. [[CrossRef](#)]
27. Ryu, Y.; Kim, W.; Koo, S.; Kang, H.; Watanabe, K.; Taniguchi, T. Interface-Confined Doubly Anisotropic Oxidation of Two-Dimensional MoS<sub>2</sub>. *Nano Lett.* **2017**, *17*, 7267–7273. [[CrossRef](#)]

28. Spychalski, W.L.; Pisarek, M.; Szoszkiewicz, R. Microscale Insight into Oxidation of Single MoS<sub>2</sub> Crystals in Air. *J. Phys. Chem. C* **2017**, *121*, 26027–26033. [[CrossRef](#)]
29. Kozbial, A.; Gong, X.; Liu, H.; Li, L. Understanding the Intrinsic Water Wettability of Molybdenum Disulfide (MoS<sub>2</sub>). *Langmuir* **2015**, *31*, 8429–8435. [[CrossRef](#)]
30. Lieber, C.M.; Kim, Y. Characterization of the structural, electronic and tribological properties of metal dichalcogenides by scanning probe microscopies. *Thin Solid Films* **1991**, *206*, 355–359. [[CrossRef](#)]
31. Szoszkiewicz, R.; Riedo, E. Nucleation time of nanoscale water bridges. *Phys. Rev. Lett.* **2005**, *95*, 135502. [[CrossRef](#)]
32. Szoszkiewicz, R.; Riedo, E. Nanoscopic friction as a probe of local phase transitions. *Appl. Phys. Lett.* **2005**, *87*, 033105. [[CrossRef](#)]
33. Maugis, D. *Contact, Adhesion and Rupture of Elastic Solids*; Springer-Verlag: Berlin, Germany, 1999; pp. 1–421.
34. Rice, R.H.; Mokarian-Tabari, P.; King, W.P.; Szoszkiewicz, R. Local Thermomechanical Analysis of a Microphase-Separated Thin Lamellar PS b PEO Film. *Langmuir* **2012**, *28*, 13503–13511. [[CrossRef](#)] [[PubMed](#)]
35. Bertolazzi, S.; Brivio, J.; Kis, A. Stretching and Breaking of Ultrathin MoS<sub>2</sub>. *ACS Nano*. **2011**, *5*, 9703–9709. [[CrossRef](#)]
36. Mortazavi, B.; Ostadhossein, A.; Rabczuk, T.; van Duin, A.C.T. Mechanical response of all-MoS<sub>2</sub> single-layer heterostructures: A ReaxFF investigation. *Phys. Chem. Chem. Phys.* **2016**, *18*, 23695–23701. [[CrossRef](#)]
37. Lince, J.R.; Frantz, P.P. Anisotropic oxidation of MoS<sub>2</sub> crystallites studied by angle-resolved X-ray photoelectron spectroscopy. *Tribol. Lett.* **2000**, *9*, 211–218. [[CrossRef](#)]
38. Guimond, S.; Göbke, D.; Sturm, J.M.; Romanyshyn, Y.; Kuhlenbeck, H.; Cavalleri, M.; Freund, H.-J. Well-Ordered Molybdenum Oxide Layers on Au(111): Preparation and Properties. *J. Phys. Chem. C* **2013**, *117*, 8746–8757. [[CrossRef](#)]
39. Zhu, H.; Qin, X.; Cheng, L.; Azcatl, A.; Kim, J.; Wallace, R.M. Remote Plasma Oxidation and Atomic Layer Etching of MoS<sub>2</sub>. *ACS Appl. Mater. Interfaces* **2016**, *8*, 19119–19126. [[CrossRef](#)]
40. Seguin, L.; Figlarz, M.; Cavagnat, R.; Lassegues, J.-C. Infrared and Raman spectra of MoO<sub>3</sub> molybdenum trioxides and MoO<sub>3</sub>·xH<sub>2</sub>O molybdenum trioxide hydrates. *Spectrochimica Acta Part A* **1995**, *51*, 1323–1344. [[CrossRef](#)]
41. Kuzmin, A.; Purans, J. Dehydration of the molybdenum trioxide hydrates MoO<sub>3</sub>·nH<sub>2</sub>O: In situ x-ray absorption spectroscopy study at the Mo K edge. *J. Phys. Cond. Matt.* **2000**, *12*, 1959–1970. [[CrossRef](#)]
42. Cruywagen, J.J.; Heyns, J.B.B. Solubility of yellow molybdenum(VI) oxide dihydrate (MoO<sub>3</sub>·2H<sub>2</sub>O) in 3,0M-sodium perchlorate at 25 °C. *S. Afr. J. Chem.* **1981**, *34*, 118–120.
43. Smolik, G.R.; Petti, D.A.; Schuetz, S.T. *Oxidation, Volatilization and Redistribution of Molybdenum from TZM Alloy in Air*; U.S. DOE Report; INEEL/EXT-99-01353; OSTI: Oak Ridge, TN, USA, 2000.
44. Castellanos-Gomez, A.; Barkelid, M.; Goossens, A.M.; Calado, V.E.; van der Zant, H.S.J.; Steele, G.A. Laser-Thinning of MoS<sub>2</sub>: On Demand Generation of a Single-Layer Semiconductor. *Nano Lett.* **2012**, *12*, 3187–3192. [[CrossRef](#)] [[PubMed](#)]
45. Sunamura, K.; Page, T.R.; Yoshida, K.; Yano, T.-A.; Hayamizu, Y. Laser-induced electrochemical thinning of MoS<sub>2</sub>. *J. Mat. Chem. C* **2016**, *4*, 3268. [[CrossRef](#)]
46. Inzani, K.; Nematollahi, M.; Vullum-Bruer, F.; Grande, T.; Reenaas, T.W.; Selbach, S.M. Electronic properties of reduced molybdenum oxides. *Phys. Chem. Chem. Phys.* **2017**, *19*, 9232. [[CrossRef](#)] [[PubMed](#)]

